ACS Sustainable Chemistry & Engineering

Research Article

pubs.acs.org/journal/ascecg

Plasmonic Bi Metal Deposition and g-C_3N_4 Coating on Bi_2WO_6 Microspheres for Efficient Visible-Light Photocatalysis

Jiajia Wang,[†,‡] Lin Tang,*[,†,‡] Guangming Zeng,*[,†,‡] Yani Liu,[†,‡] Yaoyu Zhou,[§] Yaocheng Deng,[†,‡] Jingjing Wang,[†,‡] and Bo Peng[†,‡]

[†]College of Environmental Science and Engineering, Hunan University, 8 South Lushan Road, Yuelu District, Changsha 410082, P.R. China

[‡]Key Laboratory of Environmental Biology and Pollution Control, Ministry of Education, Hunan University, 8 South Lushan Road, Yuelu District, Changsha 410082, P.R. China

[§]College of Resources and Environment, Hunan Agricultural University, 1 Agricultural University Road, Furong District, Changsha 410128, P.R. China

Supporting Information

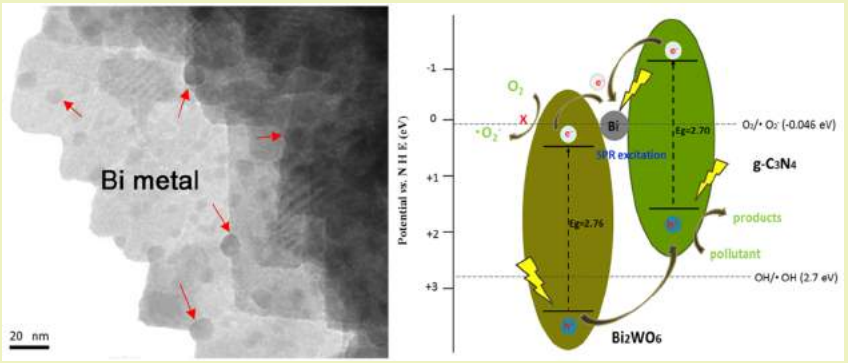

ABSTRACT: A low-cost semiconductor-based photocatalyst using visible light energy has attracted increasing interest for energy generation and environmental remediation. Herein, plasmonic Bi metal was deposited in situ in g-C_3N_4@Bi_2WO_6 microspheres via a hydrothermal method. As an electron-conduction bridge, metallic Bi was inserted as the interlayer between g-C_3N_4 and the surface of Bi_2WO_6 microspheres to enhance visible light absorption due to the surface plasmon resonance (SPR) effect and facilitate efficient electron-carrier separation. Different characterization techniques, including XRD, SEM, TEM, UV−vis, XPS, photoluminescence, and photocurrent generation, were employed to investigate the morphology and optical properties of the as-prepared samples. The results indicated that the g-C_3N_4(20%)@Bi@Bi_2WO_6 microsphere sample exhibited an extraordinary enhanced photocatalytic activity, higher than those of the g-C_3N_4, Bi_2WO_6, and g-C_3N_4(20%)@Bi_2WO_6 samples. It implies that the heterostructured combination of g-C_3N_4, metallic Bi, and Bi_2WO_6 microspheres provided synergistic photocatalytic activity via an efficient electron transfer process. On the basis of the results, a possible photocatalytic mechanism of the as-prepared samples was proposed. The present study demonstrated the feasibility of utilizing low-cost metallic Bi as a substitute for noble metals to design a doped photocatalysis composite with enhanced photocatalytic performance.

KEYWORDS: *plasmonic Bi metal, g-C_3N_4, Bi_2WO_6 microspheres, SPR effect, charge separation*

INTRODUCTION

Because of the growing concern over energy and environment issues, semiconductor-based photocatalytic hydrogen generation from water and photodegradation of organic pollutants using solar light energy have attracted increasing interest in the past years.[1,2] Visible-light-responsive photocatalysts for efficient utilization of sunlight are highly desired. There have been significant advances in the design and synthesis of visible light-responsive photocatalysts for application in organic synthesis, solar cell, water splitting, and organic contaminant degradation.[3−5] An ideal photocatalyst involving the generation of radical oxidative species induced by visible light is the key factor in the photocatalytic process. It should have a wide photoabsorption range and a low recombination rate of the photogenerated carriers. For these two issues to be addressed, the general concept is to narrow the band gap and restrain the photogenerated carrier recombination.[6−8]

Bi_2WO_6, one of the simplest aurivillius oxides, has been reported to exhibit interesting photocatalytic activities.[9−11] However, bare Bi_2WO_6 presents photoabsorption from UV to

Received: September 28, 2016
Revised: October 27, 2016
Published: November 6, 2016

DOI: 10.1021/acssuschemeng.6b02351
ACS Sustainable Chem. Eng. 2017, 5, 1062−1072

the visible light region shorter than 450 nm, which occupies a small part of the solar spectrum.[12] Moreover, fast recombination rate of electron−hole pairs significantly limits its energy conversion efficiency. Both metal/nonmetal doping and surface modification have been used to change the electronic structures and intrinsic properties of Bi_2WO_6, such as fluorinated and N-doped Bi_2WO_6 or doping Bi_2WO_6 with the noble metals Ag and CdS.[13−16] However, problems such as thermal instability, increased carrier recombination centers, and high cost of ion-implantation facility are significant challenges for these types of strategies.[17] It is true that the precious metals are of higher cost and not readily available. It is thus reasonable to consider some inexpensive metals with similar properties to be decent candidates. They should have the advantages of low price, easy availability, and good transport properties.[18]

Recently, semimetal bismuth (Bi) has been demonstrated to be an ideal substitute for noble metals.[19,20] Low-cost Bi metal has been reported to exhibit a direct plasmonic photocatalytic ability,[21−23] which may serve as a promising cocatalyst to enhance the photocatalytic efficiency of many photocatalysts. For example, Bi metal has been coupled with various photocatalysts, such as $(BiO)_2CO_3$,[24] g-C_3N_4,[25] and Bi_2MoO_6.[26] Excitingly, all of these Bi-coupled photocatalysts demonstrated obviously better photocatalytic performances. Moreover, Bi metal could also accelerate the charge-carrier separation when coupled with BiOCl, $(BiO)_2CO_3$, and Bi_2O_3.[18,19,27] All of the Bi-coupled nanocomposites described above exhibited highly enhanced photocatalytic performances. In addition, the electrical conductivity of these Bi-coupled nanocomposites increases so that the transfer rate of photogenerated carriers can be accelerated by coupling with Bi metal. Regarding the pronounced multimetal oxide nature of Bi_2WO_6, it is of great significance to clarify how Bi metal coupling influences the electronic band structure of Bi_2WO_6.

Another way to control the recombination of photogenerated carriers is to develop a heterojunction structure between two different photocatalysts with appropriate band potentials. The heterojunctions can accelerate the separation of photogenerated carriers and improve the activity of photocatalysts. Graphitic C_3N_4 (g-C_3N_4), with a band gap of ∼2.7 eV, is a promising photocatalyst for hydrogen and oxygen production from water splitting under visible light illumination.[28,29] Recently, many new functional g-C_3N_4, such as C_3N_4 thin film, C_3N_4 quantum dots, and nitrogen-doped porous carbon g-C_3N_4, have been developed.[30−32] They all exhibited a remarkably high photocatalytic activity toward water splitting. In the photocatalyst system of g-C_3N_4/Bi_2WO_6 composites, the photoinduced electrons tend to pass from the CB of g-C_3N_4 to the CB of Bi_2WO_6. However, in the case of the visible light region larger than 450 nm, Bi_2WO_6 generates fewer electrons, which results in a slow electron transfer rate from g-C_3N_4 to Bi_2WO_6.

Herein, a novel ternary composite of heterostructured g-C_3N_4@Bi@Bi_2WO_6 (CBW) has been prepared via a simple and low energy cost hydrothermal method within only 2 h. In the hydrothermal procedure, $NaBH_4$ functioned as a reductant in the reduction of Bi^{3+} to metallic Bi. In the case of the CBW composite, the main role of Bi metal was taken as follows: (i) Bi metal behaved as an "electron bridge" to accelerate the charge-carrier transfer from g-C_3N_4 to Bi_2WO_6 and (ii) the composite strongly absorbed visible light because of the surface plasmon resonance of Bi metal. The photocatalytic degradation of 2,4-dichlorophenol (2,4-DCP), methyl orange (MO), and rhodamine B (RhB) under visible light to evaluate its photocatalytic activity demonstrated that the CBW composite exhibited much more excellent photocatalytic activity.

MATERIALS AND METHODS

Synthesis of the Photocatalyst. All reagents for synthesis were chemically pure and used without further purification. The metal-free g-C_3N_4 powders were synthesized by heating melamine in a muffle furnace. In a typical procedure, 10 g of melamine was placed in an alumina crucible with a cover. The crucible was heated at 520 °C for 2 h at a heating rate of 10 °C min^{-1}. Further deammoniation reaction was conducted at 520 °C for 2 h. After cooling to room temperature, the products were ground into powders for further use.

CBW composites were obtained by a hydrothermal method with g-C_3N_4 and the precursor of Bi_2WO_6. In a typical synthesis run, appropriate amounts of g-C_3N_4 and $Bi(NO_3)_3{\cdot}5H_2O$ were added to 20 mL of deionized water, followed by vigorous magnetic stirring for 3 h to obtain a uniform suspension. Meanwhile, a stoichiometric amount of $Na_2WO_4{\cdot}2H_2O$ solid was dissolved in glacial acetic acid to obtain a clear solution. The solution was added dropwise to the suspension with Bi/W molar ratio of 2 and subsequently stirred for another 1 h at room temperature. Then, an appropriate amount of $NaBH_4$ and $NaBH_4$/$Bi(NO_3)_3{\cdot}5H_2O$ with a molar ratio of 0.2 was dropwise added into the above solution. The theoretical molar ratio of Bi_0/Bi_2WO_6 is approximately 0.13. The mixture was transferred into a 50 mL Teflon-lined autoclave to carry out the hydrothermal process at 160 °C for 2 h. Subsequently, after cooling to room temperature, the precipitate was collected by filtration, washed with ethyl alcohol and distilled water several times, and dried at 60 °C for 12 h. Finally, the obtained CBW composites were ground for further use. According to this method, C_3N_4−Bi_2WO_6 with different mass ratios of 1:10, 2:10, 1:2, and 1:1 were prepared and labeled as CBW-10, CBW-20, CBW-50, and CBW-100, respectively. The pure Bi_2WO_6 sample, g-C_3N_4(20%)@Bi_2WO_6 labeled as CW-20, and Bi@Bi_2WO_6 composites in the absence of g-C_3N_4 powder were synthesized under the same conditions.

Characterization. The phase and composition of the as-prepared samples were measured by X-ray diffraction (XRD; Rigaku, Japan) equipped with Cu Kα radiation under 40 kV and 100 mA and at a scanning rate of 4° min^{-1} with 2θ ranging from 20 to 70°. The morphologies and microstructures of the as-prepared samples were investigated by field-emission scanning electron microscopy (FESEM; FEI QUANTA200F) and transmission electron microscopy (TEM; JEOLJEM-2100F with accelerating voltage of 200 kV). The Brunauer−Emmett−Teller (BET) surface area test was performed at 77 K on a Nova 2200e surface area analyzer (Quantachrome Instruments). Fourier-transform infrared spectra (FTIR) of the samples were recorded on a Nicolet Avatar 360 (USA) instrument on samples pressed as KBr pellets. UV−vis diffuse reflectance spectra (DRS) of the samples were performed on a UV−vis spectrophotometer (Cary 300, USA) using $BaSO_4$ as reference. X-ray photoelectron spectroscopy (XPS; Thermo Fisher Scientific, UK) was employed to analyze the surface elemental composition. The photoluminescence (PL) measurements were carried out on F-7000 at room temperature.

Photoelectrochemical Measurements. The photoelectrochemical responses of the samples were measured on a CHI 660C electrochemical analyzer (CHI-660C, China) in a three-electrode cell. FTO electrodes deposited with samples served as the working electrode. A platinum foil and Ag/AgCl (3 M KCl) served as counter and reference electrodes, respectively, and 0.1 M Na_2SO_4 was used as electrolyte solution. All of the samples were analyzed without bias potential. The photoresponses of the samples were measured at 0.0 V as UV light was switched on and off. A 300 W Xe lamp with lighting wavelength range of 380−720 nm was chosen as a visible light source. All of the electrochemical measurements were carried out at room temperature.

Photocatalytic Experiment. The photocatalytic activities of CBW composites were evaluated by the decomposition of MO, RhB, and 2,4-DCP under visible light irradiation of a 300 W xenon

DOI: 10.1021/acssuschemeng.6b02351
ACS Sustainable Chem. Eng. 2017, 5, 1062−1072

lamp (CEL-HXF300; Beijing AuLight) with the 400 nm cutoff filter. In each experiment, 100 mg of catalyst was suspended in an aqueous solution (100 mL) of MO, RhB, or 2,4-DCP in a quartz glass reactor. The initial concentrations of MO, RhB, and 2,4-DCP solutions were 10, 20, and 20 mg L^{-1}, respectively. Before photocatalytic reaction, the suspension was stirred in the dark for 30 min to reach the adsorption/desorption equilibrium. At given time intervals, 4 mL of the suspension was collected and then filtered through 0.45 μm membrane filters for analysis. The concentration was analyzed by measuring the maximum absorbance at 463 nm for MO and 554 nm for RhB using a Shimadzu UV-2100 spectrophotometer. The concentration of 2,4-DCP was analyzed by high performance liquid chromatography (HPLC, Shimadzu) equipped with a UV detector (SPD-10AV) and C_{18} column (250 mm × 4.6 mm). The mobile phase was a mixture of 70/30 (v/v) acetonitrile−water mixture. The eluent was delivered at a rate of 1 mL •min^{-1}, and the wavelength for detection was 280 nm. Total organic carbon (TOC) was measured with a Shimazu TOC analyzer (TOC-VCPH).

RESULTS AND DISCUSSION

Characterization. The overall structure of the prepared samples was characterized by XRD. The XRD patterns in Figure 1 shows that the pure Bi_2WO_6 and CBW composites

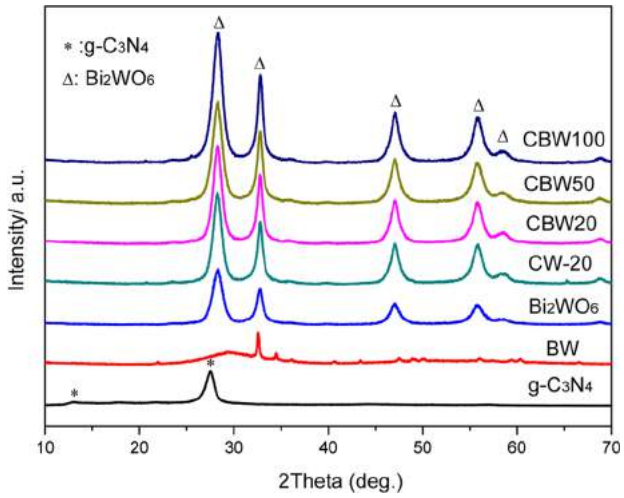

Figure 1. XRD patterns of g-C_3N_4, BW, Bi_2WO_6, CW-20, CBW-20, CBW-50, and CBW-100 samples.

exhibit similar diffraction patterns. The peaks at 2θ around 28.3°, 32.79°, 47.1°, 55.8°, 58.5°, 68.8°, 75.9°, and 78.4°, are attributed to the (131), (200), (202), (331), (262), (400), (193), and (402) crystallographic planes of orthorhombic Bi_2WO_6 (JCPDS, No. 39−0256). Two characteristic peaks of g-C_3N_4 corresponded to the (100) and (002) planes of g-C_3N_4, respectively. It is obvious that crystal of pure Bi@Bi_2WO_6 did not grow well. In pure Bi_2WO_6 precursor aqueous phase, the growth rate from the nucleus to nanoparticles during 2 h of hydrothermal reaction could not be regulated by g-C_3N_4. They might tend to aggregate into an irregular bigger ball. The Bi@Bi_2WO_6 will not be discussed in the following discussions. No typical diffraction peaks of Bi metal or g-C_3N_4 appear in the g-C_3N_4@Bi@Bi_2WO_6 composite. The reason can be ascribed to low weight loading of g-C_3N_4 or Bi metal on the surface of the Bi_2WO_6 composite, and the typical diffraction peak at 27.4° g-C_3N_4 of is too close to the peak at 28.3° of Bi_2WO_6. It might be sheltered. The same phenomena have been reported as for other kinds of metal/semiconductor composite. For instance, Xu et al. found that the characterization peaks of g-C_3N_4 could not be found when the weight ratio of g-C_3N_4 to Ag_2O in the g-C_3N_4/ Ag_2O is less than 1:1.[33] Yuan et al. found that it was difficult to find the diffraction peaks of metallic Ag in Ag/g-C_3N_4 heterostructures by XRD patterns.[34] Instead, the existence of metallic Bi in the composites can be further proved by XPS and HRTEM images.

The morphologies of the prepared samples were characterized by SEM, TEM, and HRTEM. Figure 2 shows the SEM, TEM, and HRTEM images at different magnifications. Figure 2a shows a typically aggregated morphology of the pure g-C_3N_4 samples, where large size particles (diameters of 1−4 μm) are observed. After introducing g-C_3N_4, the CBW-20 samples consist of many flowerlike hierarchical microspheres (~2.0 μm) self-assembled by nanosheets (Figure 2b and e). As shown in Figure 2c and f, though the loading amount of g-C_3N_4 increases form 20% to 50%, the diameter of CBW-50 microspheres shows no obvious change. However, the Bi metal can not be directly detected in the SEM images due to very small amount of Bi and its small particle size. On the basis of TEM observations (Figure 2h), the CBW-20 samples consist of hierarchical microspheres which have solid centers. Figure 2i shows that many uniformly distributed dots with diameters ranging from 5 to 10 nm are clearly observed upon the nanoflake unit surfaces of CBW-20, which are probably Bi nanoparticles. To obtain further information about the microstructures of these Bi nanoparticles, HRTEM analysis was employed. Figure 2k shows a typical HRTEM image of CBW-20, which is taken from the edge of a single nanosheet. The lattice spaces are 0.187 and 0.272 nm, which correspond to the (002) crystal plane of Bi_2WO_6 and (202) lattice plane of metallic Bi, respectively.[35] These results confirm the presence of metallic Bi with diameters ranging from 5 to 10 nm on the surface of Bi_2WO_6 microspheres. The light part in the above was g-C_3N_4, which further demonstrates that Bi_2WO_6 nanoflakes were well coated by g-C_3N_4. This result indicates that CBW-20 was heterogeneous in structure rather than a physical mixture of two separate phases of g-C_3N_4 and Bi_2WO_6. In addition, it should be noted that this tight coupling promoted the charge transfer rate between g-C_3N_4 and Bi_2WO_6, which was favorable for the separation of photogenerated carriers, thus improving the photocatalytic activity.[36]

The nitrogen stripping absorption curves of g-C_3N_4, Bi_2WO_6, and CBW composites are also shown in Figure S1. The BET surface areas of g-C_3N_4, Bi_2WO_6, CBW-10, CW-20, CBW-20, CBW-50 and CBW-100 are listed in Table S1. It shows that CBW composites have higher surface areas than that of pure Bi_2WO_6, which might be due to the pore volume of CBW composites changing after the addition of g-C_3N_4.

The surface chemical composition of the CBW-20 sample was conducted via XPS analysis. The XPS survey spectra of CBW-20 are shown in Figure 3. They indicate the existence of C, N, W, O, and Bi elements. Binding energies are assigned to C 1s, N 1s, W 4f, Bi 4f, W 4d, O 1s, and Bi 4p (Figure 3a). For further insight to be gained into the chemical states of C and N elements in the composite, the high resolution XPS spectra of C 1s and N 1s were measured. For C 1s spectra (Figure 3b), the two strong peaks located at 286.4 and 288.2 eV can be attributed to sp^2 C−C bonds and sp^2-hybridized carbon in N-containing aromatic rings (N−C═N), respectively.[37,38] The fitted peaks of N 1s spectra (Figure 3c), at around 398.7, 400.3, and 403.9 eV, can be assigned to the sp^2-hybridized nitrogen involved in triazine rings (C−N═C), the tertiary nitrogen N−$(C)_3$ groups, and π excitations, respectively.[37] The CBW-20

DOI: 10.1021/acssuschemeng.6b02351
ACS Sustainable Chem. Eng. 2017, 5, 1062−1072

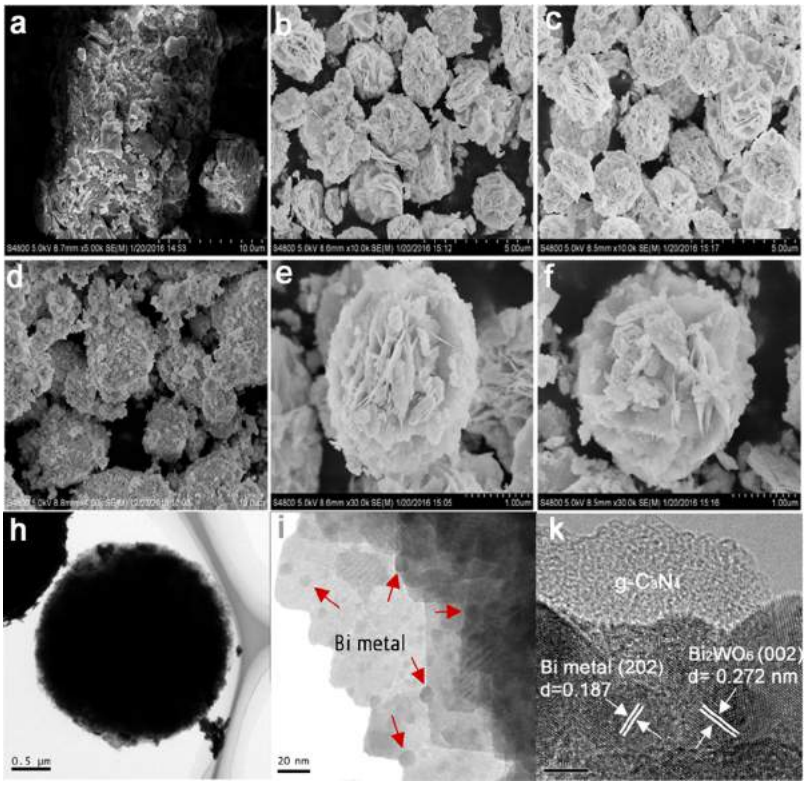

Figure 2. SEM images of (a) pure g-C_3N_4; (b, e) CBW-20; (c, f) CBW-50; (d) BW; TEM and HRTEM images of (h, i, k) CBW-20.

composite displayed ~0.6 eV shifts to higher binding energies of N 1s than that of pure g-C_3N_4. This is probably because Bi_2WO_6 hybridized with g-C_3N_4 and therefore led to the inner shift of N 1s. The C 1s peaks had only a slight shift.

The high resolution Bi 4f XPS spectra are also shown in Figure 3d. Two strong peaks at 158.8 and 164.1 eV are assigned to the binding energies of Bi 4f7/2 and Bi 4f5/2, respectively, which are the characteristics of Bi^{3+} in Bi_2WO_6.[39] In addition to the two main characteristic peaks, two tiny peaks located at 157.1 and 162.4 eV are found, which can be attributed to the metallic Bi on the surface of the Bi_2WO_6.[18] Such a similar experimental phenomenon also appeared in the work of Huang et al.[22] They found that two characteristic peaks of the metallic Bi were also very small. The possible reason for this phenomenon is probably due to the fact that the amount of reduction of Bi^{3+} to metallic Bi was very small. Figure 3e shows the XPS spectrum in the W 4f region with a binding energy at 35.4 eV for W 4f7/2 and at 37.5 eV for W 4f5/2, indicating that the existence of W was in the chemical state of W^{6+}. In Figure 3f, the O 1s spectra of CBW-20 at 530.5 and 532.5 eV are assigned to the Bi−O bonds and the hydroxyl groups, respectively.[40] The XPS results reveal the coexistence of metallic Bi deposition and g-C_3N_4-modified Bi_2WO_6.

The CBW composite microspheres were further characterized via FT-IR spectroscopy (Figure 4). The pure Bi_2WO_6 sample shows main absorption bands at 400−800 cm^{-1}, which can be assigned to Bi−O, W−O stretching, and W−O−W bridging stretching modes.[41] In the case of pure g-C_3N_4, several typical absorption peaks at 1247, 1329, 1569, and 1636 cm^{-1} correspond to the typical stretching modes of the CN heterocycles.[42] Additionally, the characteristic peak at 808 cm^{-1} is attributed to the typical bending vibration of s-triazine units.[42,43] The strong band of 3100−3300 cm^{-1} corresponds to the stretching modes of primary and secondary amines and their intermolecular hydrogen bonding interactions.[44] There is no distinct difference between CW-20 and CBW composites because the metallic Bi does not have typical absorption peaks in FT-IR spectroscopy. All characteristic absorption bands of g-C_3N_4 and Bi_2WO_6 appear in the spectra of CBW composites, indicating the coexistence of these two semiconductors.

The absorbance properties of the prepared samples were characterized using UV−vis diffuse reflectance spectroscopy. The UV−vis diffuse reflectance spectra of the prepared CBW composites are shown in Figure 5. The absorption edge of pure Bi_2WO_6 was ~450 nm, indicating that Bi_2WO_6 was less responsive to visible light. The band gap energy of pure Bi_2WO_6 was estimated to be ~2.70 eV. For pure g-C_3N_4, the basal absorption edge occurred at a wavelength of ~470 nm, corresponding to a band gap of 2.70 eV.[45] The photoabsorption of CW-20 underwent distinct enhancement in the whole visible light region. Compared to pure Bi_2WO_6, CW-20 exhibited increasing absorption in the 450−480 nm region, and the absorption edge occurred at a wavelength of ~465 nm, which was due to the presence of g-C_3N_4 on the Bi_2WO_6 microspheres. CBW-20 composites exhibit obvious visible light absorption compared to that of CW-20, and the absorption edge occurs at a wavelength longer than 500 nm, which can be attributed to the SPR effect of the loading Bi and further confirms the formation of semimetal Bi.[19] The band gap energies of semiconductors can be estimated by Kubelka−Munk transformation, $\alpha h\upsilon = A(h\upsilon - E_g)^{n/2}$, where α represents the absorption coefficient, υ is the light frequency, E_g is the band gap energy, A is a constant, and n depends on the characteristics of the transition in a semiconductor.[46] According to Kubelka−Munk transformation, E_g values of g-C_3N_4, Bi_2WO_6, and CBW-20 were calculated to be 2.70, 2.76, and 2.52 eV, respectively. E_g of CBW-20 is shown in the inset of Figure 5. The potentials of the valence band (VB) and the

DOI: 10.1021/acssuschemeng.6b02351
ACS Sustainable Chem. Eng. 2017, 5, 1062−1072

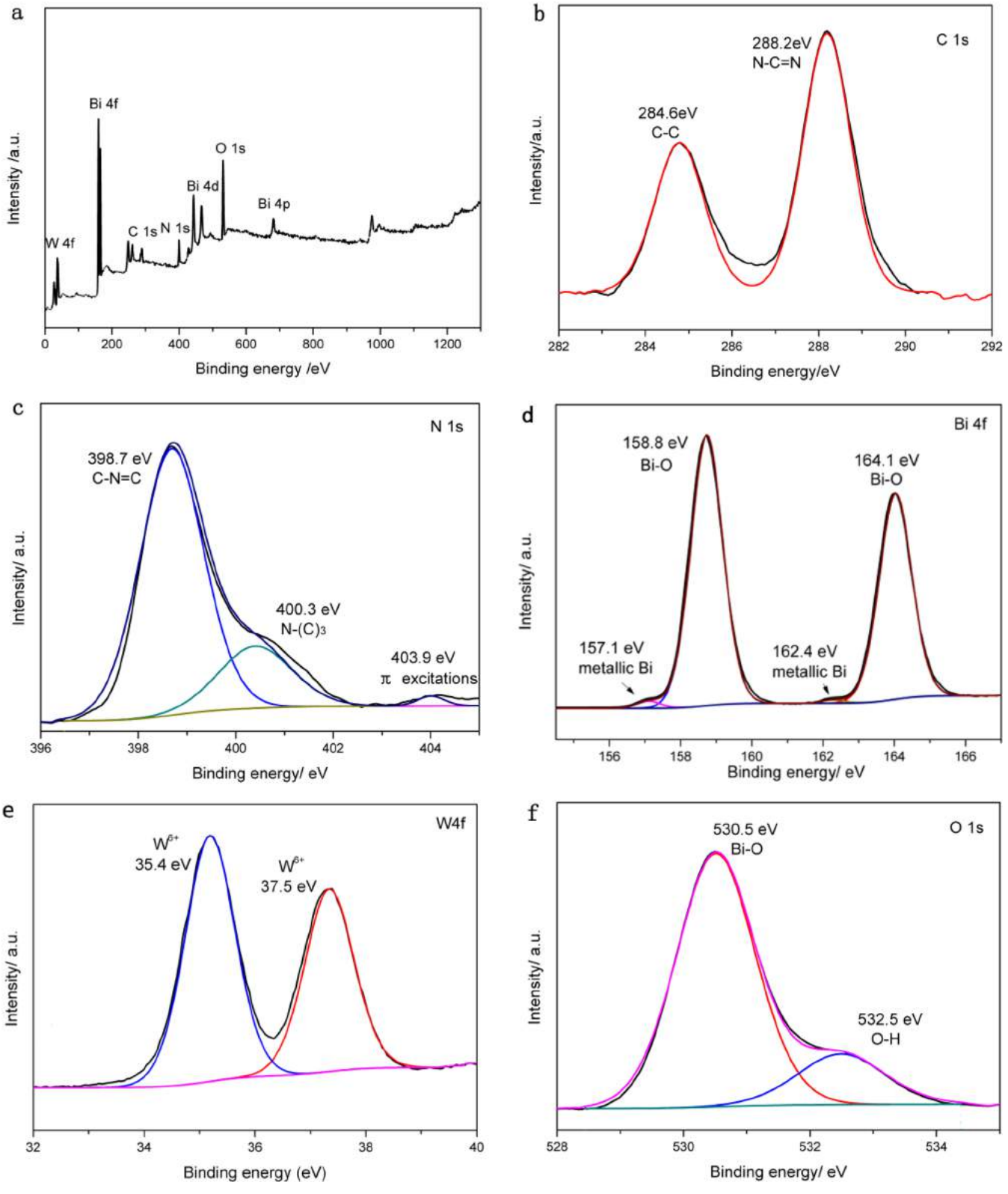

Figure 3. XPS spectra of CBW-20: (a) survey, (b) C 1s, (c) N, (d) Bi 4f, (e) W 4f, (f) O 1s.

conduction band (CB) of a semiconductor were calculated according to the empirical equations

$$E_{VB} = X - E_0 + 0.5E_g \quad (1)$$

$$E_{CB} = E_{VB} - E_g \quad (2)$$

where E_{VB} represents the valence band edge potential, X is the electronegativity of the semiconductor, which is the geometric mean of the constituent atoms, E_0 is the energy of free electrons on the hydrogen scale (~4.5 eV vs NHE), and E_g is the band gap energy of the semiconductor. The values of X for g-C_3N_4 and Bi_2WO_6 are 4.64 and 6.36 eV, respectively. The E_{VB} of g-

DOI: 10.1021/acssuschemeng.6b02351
ACS Sustainable Chem. Eng. 2017, 5, 1062−1072

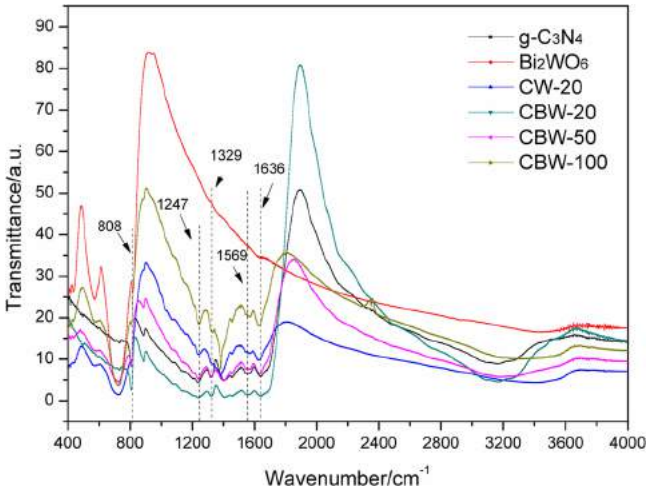

Figure 4. FT-IR spectra of pure g-C_3N_4, Bi_2WO_6, CW-20, CBW-20, CBW-50, and CBW-100 samples.

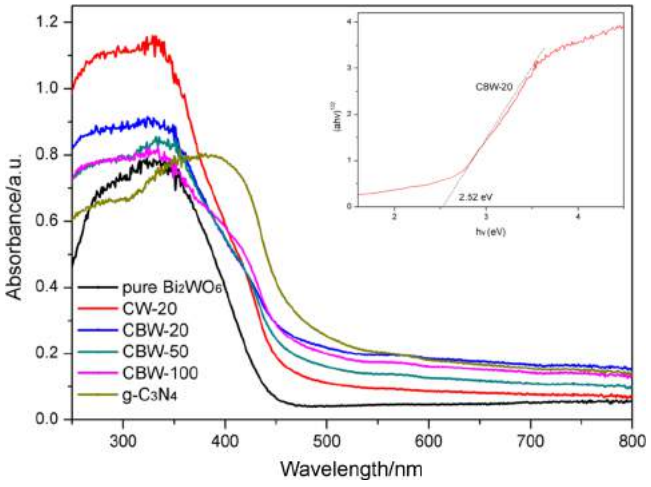

Figure 5. UV−vis spectra of pure g-C_3N_4, Bi_2WO_6, CW-20, CBW-20, CBW-50, and CBW-100 samples.

C_3N_4 and Bi_2WO_6 were calculated to be 1.49 and 3.24 eV, respectively. The E_{CB} of g-C_3N_4 and Bi_2WO_6 were estimated to be −1.21 and 0.48 eV, respectively.

The photoresponses of g-C_3N_4, Bi_2WO_6, CW-20, and CBW-20 electrodes were tested, and Figure 6 shows fast and uniform photocurrent responses of g-C_3N_4, Bi_2WO_6, CW-20, and CBW-20. After hybridization with metallic Bi and g-C_3N_4, the photocurrent of Bi_2WO_6 was promoted to be ∼2 times higher than that of pure Bi_2WO_6 under visible light irradiation. The photocurrent enhancement of CBW-20 was attributed to enhanced photogenerated carrier separation. The photocurrent enhancement of CBW-20 was much higher than that of CW-20, which suggests that the introduction of metallic Bi has a significant effect on the electronic properties of CW-20.

We also employed photoluminescence (PL) emission to investigate the generation, transfer, and recombination of charge carriers. Figure 7 shows the room-temperature PL spectra of g-C_3N_4, CW-20, and CBW-20. All of the prepared samples exhibited a broad emission peak at around 460 nm, which is consistent with UV−vis DRS analysis. Generally, a lower PL intensity is indicative of a lower photogenerated carrier recombination rate. Obviously, CBW-20 shows significantly diminished PL intensity compared with those of

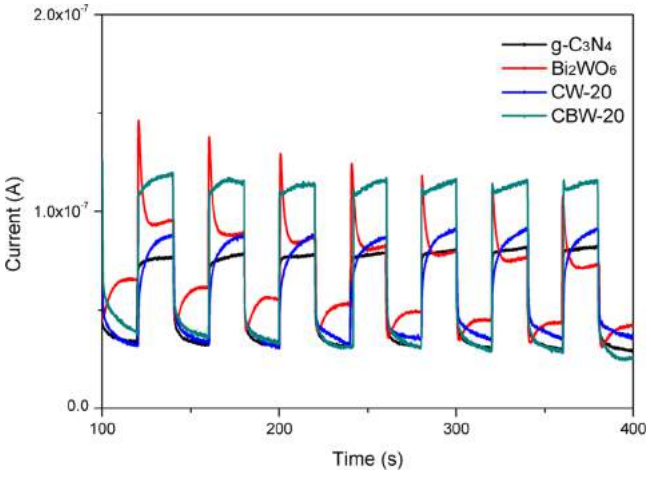

Figure 6. Photocurrent responses of g-C_3N_4, Bi_2WO_6, CW-20, and CBW-20 samples.

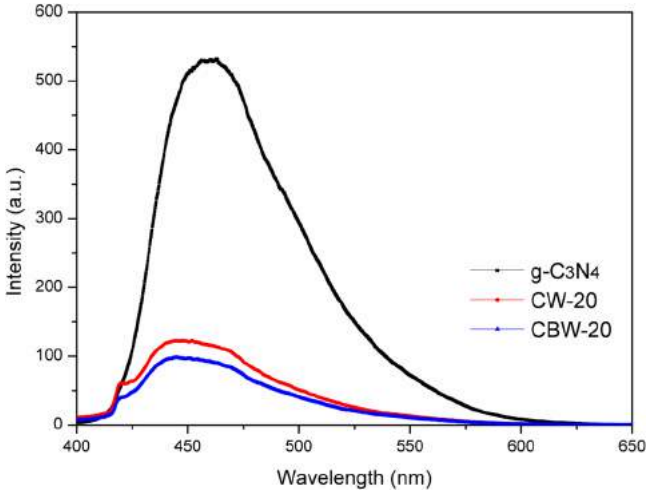

Figure 7. PL spectra of g-C_3N_4, Bi_2WO_6, and CBW-20.

pure g-C_3N_4 and CW-20, indicating that the deposition of Bi led to an obvious increase in the separation efficiency of electron−hole pairs. This result might be derived from the fact that metallic Bi connecting g-C_3N_4 with Bi_2WO_6 is beneficial for promoting carrier separation and therefore hindering the charge recombination.

Photocatalytic Activity of g-C_3N_4@Bi@Bi_2WO_6 Composite. The photocatalytic activity of CBW composites was tested by the degradation of MO, RhB, and 2,4-DCP under visible light irradiation. The degradation curves of MO are shown in Figure 8a. Bi_2WO_6 had only little degradation to MO. As for pure g-C_3N_4, it also showed poor activity. The mechanically mixed g-C_3N_4 (20%) and Bi_2WO_6 exhibited a slight increase of photocatalytic efficiency compared with those of pure Bi_2WO_6 and g-C_3N_4. Interestingly, after coating 20% g-C_3N_4 on Bi_2WO_6, CW-20 displayed significantly enhanced degradation efficiency of MO, which reached ∼50% after irradiation for 120 min. The photocatalytic activity of CBW-20 could reach ∼70% after irradiation for 120 min. As expected, metallic Bi deposition on the g-C_3N_4-modified Bi_2WO_6 surface further improved the photocatalytic activity of the composite. The CBW-20 sample exhibited the most efficient photocatalytic performance, which was ∼16 times higher than that of the pure Bi_2WO_6 sample. However, with the loading amount of g-C_3N_4

DOI: 10.1021/acssuschemeng.6b02351
ACS Sustainable Chem. Eng. 2017, 5, 1062−1072

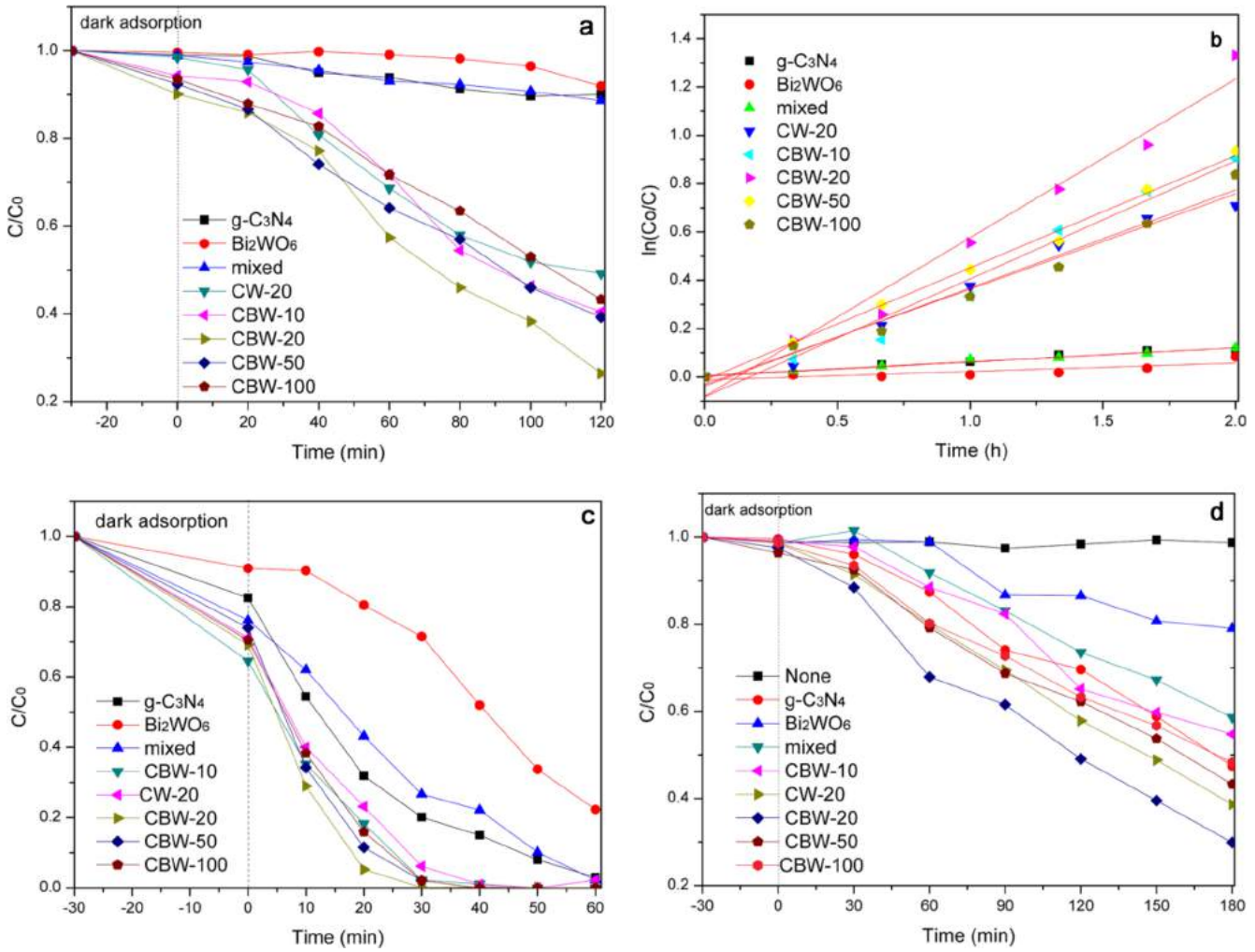

Figure 8. (a) Photodegradation of MO by using pure g-C_3N_4, Bi_2WO_6, CW-20, and CBW composites under visible light irradiation. (b) Variation in the normalized $\ln(C_0/C)$ of the MO concentration as a function of irradiation time. (c) Photodegradation of RhB under visible light irradiation. (d) Photodegradation of 2,4-DCP under visible light irradiation.

increasing to 100%, the photocatalytic activity decreased, which is probably due to the large amount of g-C_3N_4 covering the active sites of g-C_3N_4@Bi@Bi_2WO_6. These results reveal the synergic effect between g-C_3N_4 and Bi@Bi_2WO_6 in which Bi metal plays an important role in the separation of electron−hole pairs.

For the photodegradation rate of the photocatalysts to be investigated quantitatively, the pseudo-first-order equation was used, which can be expressed by eq 3.

$$\ln(C_0/C) = kt \tag{3}$$

where t, C_0, and C are the reaction time, initial MO concentration (mg/L), MO concentration at time t (mg/L), respectively, and k represents the apparent pseudo-first-order rate constant (h^{-1}). On the basis of this equation, the value of k for the pure g-C_3N_4, Bi_2WO_6, CBW-10, CW-20, CBW-20, CBW-50, and CBW-100 samples are calculated as 0.05, 0.03, 0.48, 0.39, 0.65, 0.46, and 0.40 h^{-1}, respectively. Surface-area-normalized rate constants (k_{SA}) can be calculated according to the equation $k_{obs} = k_{SA}a_s\rho_m$, where a_s is the specific surface area of the catalysts (m^2 g^{-1}), and ρ_s represents the mass concentration of the catalysts (g L^{-1} of solution). The k_{SA} values for pure g-C_3N_4, Bi_2WO_6, CBW-10, CW-20, CBW-20, CBW-50, and CBW-100 were calculated to be approximately 4.5×10^{-3}, 1.4×10^{-3}, 1.9×10^{-2}, 1.5×10^{-2}, 2.3×10^{-2}, 1.4×10^{-2}, and 1.4×10^{-2} L h^{-1} m^{-2}, respectively. The highest photocatalytic rate of CBW-20 is approximately 16 times higher than that of pure Bi_2WO_6.

For the enhanced photocatalytic properties of CBW to be further confirmed, the degradation of RhB and 2,4-DCP by CBW composites were also conducted. In contrast to pure Bi_2WO_6, the CBW exhibited evidently improved photocatalytic activity toward the degradation of RhB and 2,4-DCP (Figure 8b,c). The results are similar to the photocatalytic degradation of MO. The photocatalytic experiment of 2,4-DCP by hydrothermally treated g-C_3N_4 was also conducted. According to the results, the photocatalytic degradation efficiency of 2,4-DCP by the hydrothermally treated g-C_3N_4 reached ~41.7% after 3 h of visible light irradiation, which was 6% higher than that of the raw g-C_3N_4 (shown in Figure S2). The slight influence of the hydrothermal treatment on the photocatalytic activity of g-C_3N_4 for 2,4-DCP can be ignored compared with the synergetic effect of g-C_3N_4, Bi metal, and Bi_2WO_6. This evidence apparently demonstrates that the photocatalytic activities of Bi_2WO_6 are highly improved by the comodification of metallic Bi and g-C_3N_4. In addition, the carbonization experiment of 2,4-DCP by CBW-20 was conducted. It was found that the TOC value of 2,4-DCP decreased by ~31.5%

DOI: 10.1021/acssuschemeng.6b02351
ACS Sustainable Chem. Eng. 2017, 5, 1062−1072

after 8 h of visible light irradiation, which indicates that RhB mineralization by the CBW composites is possible (shown in Figure S3).

For testing the stability of CBW-20, four consecutive runs were carried out for photocatalytic degradation of 2,4-DCP under visible light irradiation. As shown in Figure 9, the

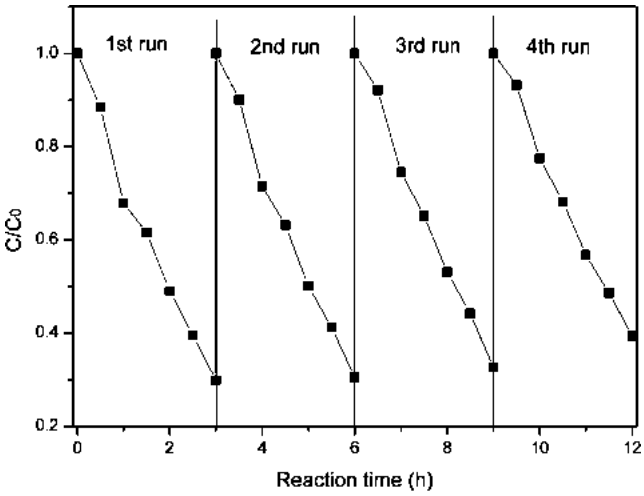

Figure 9. Recycling photocatalytic tests of CBW-20 for degradation of 2,4-DCP under visible light irradiation.

degradation efficiency of 2,4-DCP remained at 60% after the fourth cycle. The results indicate that CBW-20 is durable and stable in the photocatalytic degradation process. The sample (CBW-20) before and after the photocatalytic reaction were characterized by XRD and XPS analysis (Figure 10a,b). It was found that the XRD and XPS patterns of the recycled CBW-20 nanocomposite after four times of photocatalytic reaction had almost no obvious discrepancy compared with the fresh one. The XRD and XPS analysis of the recycled CBW-20 nanocomposite demonstrates that the properties of the as-prepared photocatalysts are stable.

Photocatalytic Mechanisms. In general, the high adsorption ability is related to high specific surface area, which might improve the photocatalytic activity of photocatalyst composites.[47] In the present work, however, the photocatalytic activities of the photocatalyst composites were not proportional to their BET surface areas. It suggests that the photocatalytic activity of CBW composites is more determined by the optical and electrical properties of photocatalysts rather than their adsorption ability.

On the basis of the results and discussion above, a possible photocatalytic mechanism for the CBW composites was proposed and schematically exhibited in Scheme 1. First, the surface plasmonic resonance of metallic Bi could significantly enhance visible light absorption, which was proven by UV−vis analysis. Second, metallic Bi was deposited on the surface of Bi_2WO_6 microspheres and functioned as an electron-conduction bridge, which played an important role in the electron transfer. The Fermi level (vs NHE) of Bi is approximately −0.17 eV.[20] Because the CB edge potential of g-C_3N_4 (−1.21 eV) is more negative than those of Bi and Bi_2WO_6 (0.48 eV), the photogenerated electrons on g-C_3N_4 could transfer to the CB of Bi_2WO_6. In such a way, the photoexcited electrons and holes could be efficiently separated, which reduced the recombination of electron−hole pairs, and

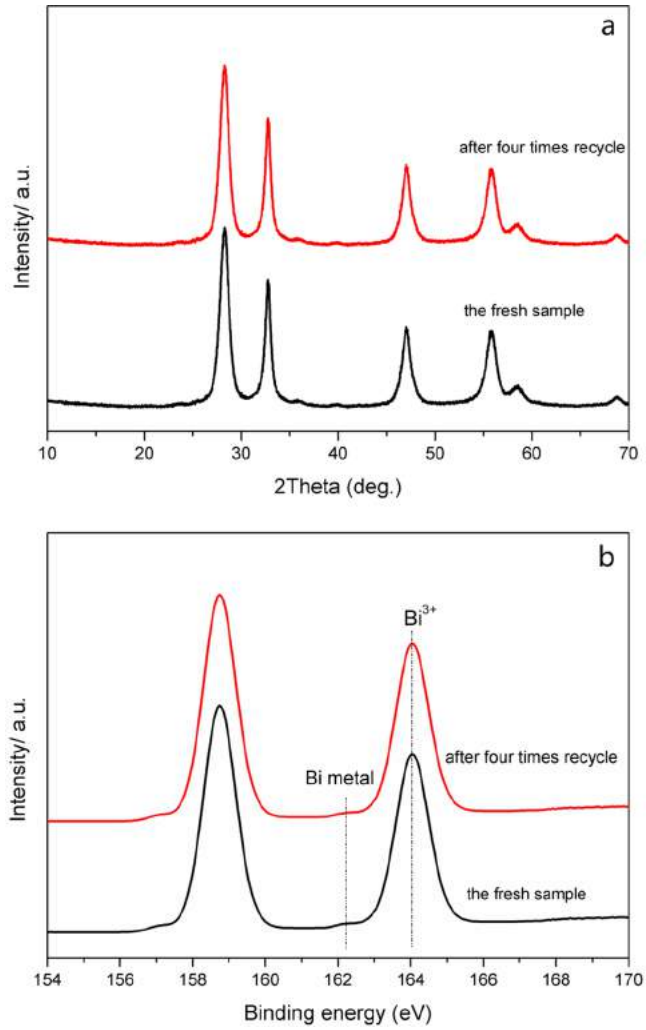

Figure 10. (a) XRD patterns of the fresh and used CBW-20 nanocomposite. (b) XPS patterns of the fresh and used CBW-20 nanocomposite.

thus, the photocatalytic activity was enhanced. The separation of electron holes between Bi_2WO_6 and g-C_3N_4 would be more efficient due to the Schottky barrier at the interface of metallic Bi and Bi_2WO_6 microspheres.[48] However, the separated electrons could not reduce O_2 to $\bullet O^{2-}$ due to the fact that the redox potential of O_2 to $\bullet O^{2-}$ (−0.33 eV) is more negative than that of the CB of Bi_2WO_6 (0.48 eV). It was proposed that the main active species were h^+ and •OH during the photodegradation process. It is also true that the content of g-C_3N_4 in CBW microspheres should be optimized, because the main degradation process happened on the surface of Bi_2WO_6, whereas the pollutant molecules had to travel through the outer layer composed of g-C_3N_4. If the outer layer g-C_3N_4 is too thick, it will retard the pollutant molecules reacting with h^+ on the surface of Bi_2WO_6. Therefore, the higher content of g-C_3N_4 led to a lower photocatalytic activity.

For evaluating the main active species generated during the photodegradation process, different scavengers, benzoquinone (BQ, 2 mM), isopropanol (IPA 10 mM), and triethanolamine (EDTA, 10 mM) were added to the photodegradation of 2,4-DCP as quenchers of three active species: superoxide radicals ($\bullet O_2^-$), hydroxyl radicals (•OH), and holes (h^+), respectively. Figure 11 shows that the photocatalytic degradation of 2,4-

DOI: 10.1021/acssuschemeng.6b02351
ACS Sustainable Chem. Eng. 2017, 5, 1062−1072

Scheme 1. Photocatalytic Mechanism Scheme of CBW Microspheres under Visible Light Irradiation (>420 nm)

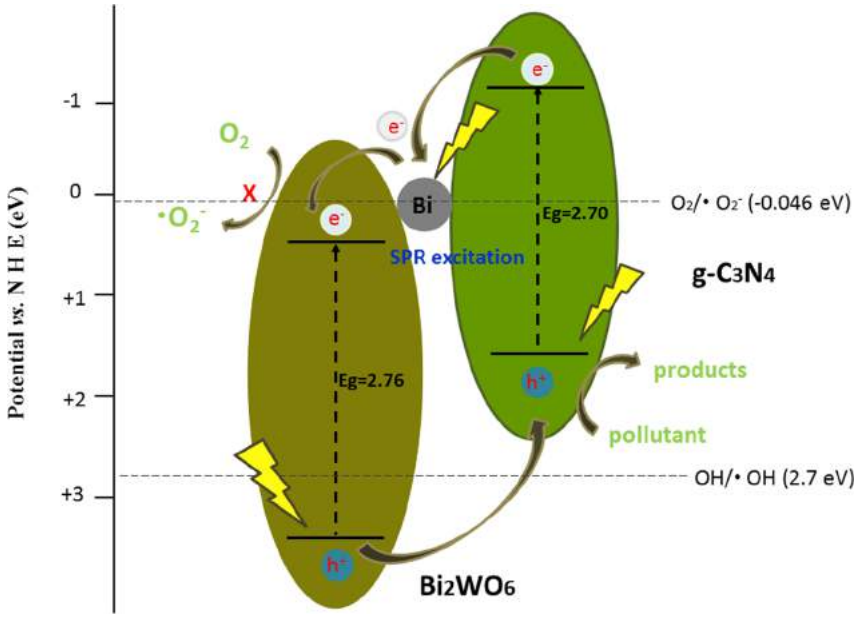

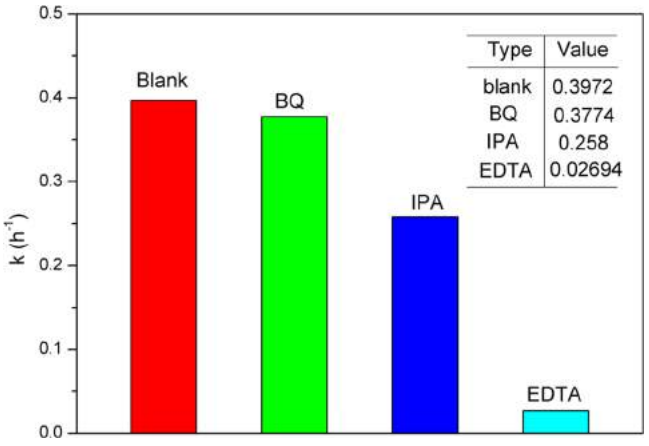

Figure 11. Photodegradation efficiency of 2,4-DCP on CBW-20 by adding the active species capture.

DCP was significantly inhibited by adding EDTA and slightly hindered after the addition of IPA. The adsorption experiment was conducted. CBW microspheres had little adsorption effect on 2,4-DCP. It demonstrates that h^+ is the most critical species, and •OH served as a secondary active species during photocatalytic degradation of 2,4-DCP.

CONCLUSIONS

In summary, we have successfully developed a Bi cocatalyst deposited g-C_3N_4@Bi_2WO_6 composite via a hydrothermal method with $NaBH_4$ acting as reductant. The metallic Bi deposited on the surface of Bi_2WO_6 microspheres in the CBW composite functioned as an electron-conduction bridge and enhanced visible light absorption of CBW. The enhanced photocatalytic activity of CBW was attributed to the cooperative contribution of SPR effects and efficient separation of photogenerated carriers by metallic Bi. CBW-20 exhibited an extraordinarily high photocatalytic activity in degradation of MO under visible light irradiation, which is ~16 times higher than that of Bi_2WO_6. On the basis of the calculated energy band positions, the mechanism of enhanced photocatalytic activity for the CBW composite was discussed, which demonstrates that h^+ is the most critical species and •OH serves as a secondary active species during the photocatalytic degradation process. Such a composite will be a promising photocatalyst for the application of environmental remediation and water purification.

ASSOCIATED CONTENT

Supporting Information

The Supporting Information is available free of charge on the ACS Publications website at DOI: 10.1021/acssuschemeng.6b02351.

N_2 adsorption−desorption isotherms and specific surface area of the prepared samples, photocatalytic degradation of 2,4-DCP by hydrothermally treated g-C_3N_4, and 2,4-DCP and TOC removal during the photocatalytic degradation (PDF)

AUTHOR INFORMATION

Corresponding Authors

*Tel: +86-731-88822778. E-mail: tanglin@hnu.edu.cn.
*Tel: +86-731-88823701. E-mail: zgming@hnu.edu.cn.

ORCID

Lin Tang: 0000-0001-6996-7955

Notes

The authors declare no competing financial interest.

ACKNOWLEDGMENTS

The study was financially supported by the National Program for Support of Top-Notch Young Professionals of China (2012), Projects 51579096, 51222805, 51521006, 51679084, and 51508175 supported by the National Natural Science Foundation of China, and the Program for New Century Excellent Talents in University from the Ministry of Education of China (NCET-11-0129).

DOI: 10.1021/acssuschemeng.6b02351
ACS Sustainable Chem. Eng. 2017, 5, 1062−1072

REFERENCES

(1) Hagfeldt, A.; Graetzel, M. Light-induced redox reactions in nanocrystalline systems. *Chem. Rev.* **1995**, *95*, 49−68.

(2) Zhang, Y.; Zeng, G. M.; Tang, L.; Huang, D. L.; Jiang, X. Y.; Chen, Y. N. A hydroquinone biosensor based on immobilizing laccase to modified core-shell magnetic nanoparticles supported on carbon paste electrode. *Biosens. Bioelectron.* **2007**, *22*, 2121−2126.

(3) Zhang, S. W.; Li, J. X.; Zeng, M.; Zhao, G. X.; Xu, J. Z.; Hu, W. P.; Wang, X. K. In situ synthesis of water-soluble magnetic graphitic carbon nitride photocatalyst and its synergistic catalytic performance. *ACS Appl. Mater. Interfaces* **2013**, *5*, 12735−12743.

(4) Zhang, S. W.; Li, J. X.; Wang, X. K.; Huang, Y. S.; Zeng, M.; Xu, J. Z. In situ ion exchange synthesis of strongly coupled Ag@ AgCl/g-C_3N_4 porous nanosheets as plasmonic photocatalyst for highly efficient visible light photocatalysis. *ACS Appl. Mater. Interfaces* **2014**, *6*, 22116−22125.

(5) Zhang, S. W.; Fan, Q. H.; Gao, H. H.; Huang, Y. S.; Liu, X.; Li, J. X.; Xu, X. J.; Wang, X. K. Formation of Fe_3O_4@MnO_2 ball-in-ball hollow spheres as a high performance catalyst with enhanced catalytic performances. *J. Mater. Chem. A* **2016**, *4*, 1414−1422.

(6) Georgieva, J.; Armyanov, S.; Valova, E.; Poulios, I.; Sotiropoulos, S. Enhanced photocatalytic activity of electrosynthesised tungsten trioxide−titanium dioxide bi-layer coatings under ultraviolet and visible light illumination. *Electrochem. Commun.* **2007**, *9*, 365−370.

(7) Lianos, P. Production of electricity and hydrogen by photocatalytic degradation of organic wastes in a photoelectrochemical cell: the concept of the photofuelcell: a review of a re-emerging research field. *J. Hazard. Mater.* **2011**, *185*, 575−590.

(8) Tang, L.; Deng, Y. C.; Zeng, G. M.; Hu, W.; Wang, J. J.; Zhou, Y. Y.; Wang, J.; Tang, J.; Fang, W. CdS/Cu_2S co-sensitized TiO_2 branched nanorod arrays of enhanced photoelectrochemical properties by forming nanoscale heterostructure. *J. Alloys Compd.* **2016**, *662*, 516−527.

(9) Zhang, Z. J.; Wang, W. Z.; Yin, W. Z.; Shang, M.; Wang, L.; Sun, S. M. Inducing photocatalysis by visible light beyond the absorption edge: effect of upconversion agent on the photocatalytic activity of Bi_2WO_6. *Appl. Catal., B* **2010**, *101*, 68−73.

(10) Zhang, L. S.; Wang, H. L.; Chen, Z. G.; Wong, P. K.; Liu, J. S. Bi_2WO_6 micro/nano-structures: synthesis, modifications and visible light-driven photocatalytic applications. *Appl. Catal., B* **2011**, *106*, 1−13.

(11) Tang, L.; Wang, J. J.; Zeng, G. M.; Liu, Y. N.; Deng, Y. C.; Zhou, Y. Y.; Tang, J.; Wang, J. J.; Guo, Z. Enhanced photocatalytic degradation of norfloxacin in aqueous Bi_2WO_6 dispersions containing nonionic surfactant under visible light irradiation. *J. Hazard. Mater.* **2016**, *306*, 295−304.

(12) Zhu, S. B.; Xu, T. G.; Fu, H. B.; Zhao, J. C.; Zhu, Y. F. Synergetic effect of Bi_2WO_6 photocatalyst with C_{60} and enhanced photoactivity under visible irradiation. *Environ. Sci. Technol.* **2007**, *41*, 6234−6239.

(13) Fu, H. B.; Zhang, S. B.; Xu, T. G.; Zhu, Y. F.; Chen, J. M. Photocatalytic degradation of RhB by fluorinated Bi_2WO_6 and distributions of the intermediate products. *Environ. Sci. Technol.* **2008**, *42*, 2085−2091.

(14) Shang, M.; Wang, W. Z.; Zhang, L.; Xu, H. Bi_2WO_6 with significantly enhanced photocatalytic activities by nitrogen doping. *Mater. Chem. Phys.* **2010**, *120*, 155−159.

(15) Yu, H. G.; Liu, R.; Wang, X. F.; Wang, P.; Yu, J. G. Enhanced visible light photocatalytic activity of Bi_2WO_6 nanoparticles by Ag_2O cocatalyst. *Appl. Catal., B* **2012**, *111*, 326−333.

(16) Ge, L.; Liu, J. Efficient visible light-induced photocatalytic degradation of methyl orange by QDs sensitized CdS-Bi_2WO_6. *Appl. Catal., B* **2011**, *105*, 289−297.

(17) Asahi, R. Y.; Morikawa, T. A.; Ohwaki, T.; Aoki, K.; Taga, Y. Visible-light photocatalysis in nitrogen-doped titanium oxides. *Science* **2001**, *293*, 269−271.

(18) Liu, X. W.; Cao, H. Q.; Yin, J. F. Generation and photocatalytic activities of Bi@Bi_2O_3 microspheres. *Nano Res.* **2011**, *4*, 470−482.

(19) Weng, S. X.; Chen, B. B.; Xie, L. Y.; Zheng, Z. Y.; Liu, P. Facile in situ synthesis of a Bi/BiOCl nanocomposite with high photocatalytic activity. *J. Mater. Chem. A* **2013**, *1*, 3068−3075.

(20) Dong, F.; Li, Q. Y.; Sun, Y. J.; Ho, W. K. Noble metal-like behavior of plasmonic Bi particles as a cocatalyst deposited on $(BiO)_2CO_3$ microspheres for efficient visible light photocatalysis. *ACS Catal.* **2014**, *4*, 4341−4350.

(21) Sun, Y. J.; Zhao, Z. W.; Dong, F.; Zhang, W. Mechanism of visible light photocatalytic NOx oxidation with plasmonic Bi cocatalyst-enhanced $(BiO)_2CO_3$ hierarchical microspheres. *Phys. Chem. Chem. Phys.* **2015**, *17*, 10383−10390.

(22) Yu, S. X.; Huang, H. W.; Dong, F.; Li, M.; Tian, N.; Zhang, T. R.; Zhang, Y. H. Synchronously Achieving Plasmonic Bi Metal Deposition and I−Doping by Utilizing $BiOIO_3$ as the Self-Sacrificing Template for High-Performance Multifunctional Applications. *ACS Appl. Mater. Interfaces* **2015**, *7*, 27925−27933.

(23) Dong, F.; Xiong, T.; Sun, Y. J.; Zhao, Z. W.; Zhou, Y.; Feng, X.; Wu, Z. B. A semimetal bismuth element as a direct plasmonic photocatalyst. *Chem. Commun.* **2014**, *50*, 10386−10389.

(24) Xiong, T.; Dong, X. A.; Huang, H. W.; Cen, W. L.; Zhang, Y. H.; Dong, F. Single precursor mediated-synthesis of Bi Semimetal deposited N-doped $(BiO)_2CO_3$ superstructures for highly promoted photocatalysis. *ACS Sustainable Chem. Eng.* **2016**, *4*, 2969−2979.

(25) Dong, F.; Zhao, Z. W.; Sun, Y. X.; Zhang, Y. X.; Yan, S.; Wu, Z. B. An advanced semimetal−organic Bi spheres−g-C_3N_4 nanohybrid with SPR-enhanced visible light photocatalytic performance for NO purification. *Environ. Sci. Technol.* **2015**, *49*, 12432−12440.

(26) Zhao, Z. W.; Zhang, W. D.; Sun, Y. J.; Yu, J. Y.; Zhang, Y. X.; Wang, H.; Dong, F.; Wu, Z. B. Bi Cocatalyst/Bi_2MoO_6 Microspheres nanohybrid with SPR-promoted visible light photocatalysis. *J. Phys. Chem. C* **2016**, *120*, 11889−11898.

(27) Wang, Z.; Jiang, C. N.; Huang, R.; Peng, H.; Tang, X. D. Investigation of optical and photocatalytic properties of bismuth nanospheres prepared by a facile thermolysis method. *J. Phys. Chem. C* **2013**, *118*, 1155−1160.

(28) Xu, L.; Huang, W. Q.; Wang, L. L.; Tian, Z. A.; Hu, W.; Ma, Y.; Wang, X.; Pan, A.; Huang, G. F. Insights into enhanced visible light photocatalytic hydrogen evolution of g-C_3N_4 and highly reduced graphene oxide composite: the role of oxygen. *Chem. Mater.* **2015**, *27*, 1612−1621.

(29) Ye, C.; Li, J. X.; Li, Z. J.; Li, X. B.; Fan, X. B.; Zhang, L. P.; Chen, B.; Tung, C. H.; Wu, L. Z. Enhanced driving force and charge separation efficiency of protonated g-C_3N_4 for photocatalytic O_2 Evolution. *ACS Catal.* **2015**, *5*, 6973−6979.

(30) Zhang, J. S.; Zhang, M. W.; Lin, L. H.; Wang, X. C. Sol processing of conjugated carbon nitride powders for thin-film fabrication. *Angew. Chem., Int. Ed.* **2015**, *54*, 6297−6301.

(31) Chen, X.; Liu, Q.; Wu, Q. L.; Du, P. W.; Zhu, J.; Dai, S. Y.; Yang, S. F. Polymer solar cells: incorporating graphitic carbon nitride (g-C_3N_4) quantum dots into bulk-heterojunction polymer solar cells leads to efficiency enhancement. *Adv. Funct. Mater.* **2016**, *26*, 1851−1851.

(32) Yu, H. J.; Shang, L.; Bian, T.; Shi, R.; Waterhouse, G. I.; Zhao, Y. F.; Zhou, C.; Wu, L. Z.; Tung, C. H.; Zhang, T. Nitrogen-doped porous carbon canosheets templated from g-C_3N_4 as metal-free electrocatalysts for efficient oxygen reduction reaction. *Adv. Mater.* **2016**, *28*, 5080−5086.

(33) Xu, M.; Han, L.; Dong, S. J. Facile fabrication of highly efficient g-C_3N_4/Ag_2O heterostructured photocatalysts with enhanced visible light photocatalytic activity. *ACS Appl. Mater. Interfaces* **2013**, *5*, 12533−12540.

(34) Yang, Y. X.; Guo, Y. N.; Liu, F. Y.; Yuan, X.; Guo, Y. H.; Zhang, S. Q.; Guo, W.; Huo, M. Preparation and enhanced visible light photocatalytic activity of silver deposited graphitic carbon nitride plasmonic photocatalyst. *Appl. Catal., B* **2013**, *142*, 828−837.

(35) Wang, W. Z.; Poudel, B.; Ma, Y.; Ren, Z. F. Shape control of single crystalline bismuth nanostructures. *J. Phys. Chem. B* **2006**, *110*, 25702−25706.

DOI: 10.1021/acssuschemeng.6b02351
ACS Sustainable Chem. Eng. 2017, 5, 1062−1072

(36) Shi, H. F.; Chen, G. Q.; Zhang, C. L.; Zou, Z. G. Polymeric g-C_3N_4 coupled with $NaNbO_3$ nanowires toward enhanced photocatalytic reduction of CO_2 into renewable fuel. *ACS Catal.* **2014**, *4*, 3637−3643.
(37) Li, J. H.; Shen, B.; Hong, Z. H.; Lin, B.; Gao, B. F.; Chen, Y. L. A facile approach to synthesize novel oxygen-doped g-C_3N_4 with superior visible light photoreactivity. *Chem. Commun.* **2012**, *48*, 12017−12019.
(38) Wang, J. C.; Yao, H. C.; Fan, Z. Y.; Zhang, L.; Wang, J. S.; Zang, S. Q.; Li, Z. J. Indirect Z-scheme BiOI/g-C_3N_4 Photocatalysts with Enhanced Photoreduction CO_2 Activity under Visible Light Irradiation. *ACS Appl. Mater. Interfaces* **2016**, *8*, 3765−3775.
(39) Tian, J.; Sang, Y. H.; Yu, G. W.; Jiang, H. D.; Mu, X. N.; Liu, H. A Bi_2WO_6 based hybrid photocatalyst with broad spectrum photocatalytic properties under UV, Visible, and Near-Infrared irradiation. *Adv. Mater.* **2013**, *25*, 5075−5080.
(40) Wu, J.; Duan, F.; Zheng, Y.; Xie, Y. Synthesis of Bi_2WO_6 nanoplate-built hierarchical nest-like structures with visible light-induced photocatalytic activity. *J. Phys. Chem. C* **2007**, *111*, 12866−12871.
(41) Yu, J. G.; Xiong, J. F.; Cheng, B.; Yu, Y.; Wang, J. B. Hydrothermal preparation and visible light photocatalytic activity of Bi_2WO_6 powders. *J. Solid State Chem.* **2005**, *178*, 1968−1972.
(42) Yan, S. C.; Li, Z. S.; Zou, Z. G. Photodegradation performance of g-C_3N_4 fabricated by directly heating melamine. *Langmuir* **2009**, *25*, 10397−10401.
(43) Tang, L.; Zeng, G. M.; Shen, G. L.; Li, Y. Rapid detection of picloram in agricultural field samples using a disposable immunomembrane-based electrochemical sensor. *Environ. Sci. Technol.* **2008**, *42*, 1207−1212.
(44) Lotsch, B. V.; Schnick, W. From triazines to heptazines: novel nonmetal tricyanomelaminates as precursors for graphitic carbon nitride materials. *Chem. Mater.* **2006**, *18*, 1891−1900.
(45) Li, Y. F.; Fang, L.; Jin, R. X.; Yang, Y.; Fang, X.; Xing, Y.; Song, S. Y. Preparation and enhanced visible light photocatalytic activity of novel g-C_3N_4 nanosheets loaded with Ag_2CO_3 nanoparticles. *Nanoscale* **2015**, *7*, 758−764.
(46) Tauc, J. Absorption edge and internal electric fields in amorphous semiconductors. *Mater. Res. Bull.* **1970**, *5*, 721−729.
(47) Liu, B.; Liu, L. M.; Lang, X. F. Doping high-surface-area mesoporous TiO_2 microspheres with carbonate for visible light hydrogen production. *Energy Environ. Sci.* **2014**, *7*, 2592−2597.
(48) Chai, B.; Peng, T. Y.; Mao, J.; Li, K.; Zan, L. Graphitic carbon nitride g-C_3N_4−Pt-TiO_2 nanocomposite as an efficient photocatalyst for hydrogen production under visible light irradiation. *Phys. Chem. Chem. Phys.* **2012**, *14*, 16745−16752.

DOI: 10.1021/acssuschemeng.6b02351
ACS Sustainable Chem. Eng. 2017, 5, 1062−1072